Microfluidic rectifier for polymer solutions flowing through porous media

Kawale, Durgesh; Jayaraman, Jishnu; Boukany, Pouyan E.

DOI
10.1063/1.5050201

Publication date
2019

Document Version
Accepted author manuscript

Published in
Biomicrofluidics

AUTHOR QUERY FORM

AIP Publishing	**Journal: Biomicrofluidics** **Article Number: 013901BMF**	**Please provide your responses and any corrections by annotating this PDF and uploading it to AIP's eProof website as detailed in the Welcome email.**

Dear Author,

Below are the queries associated with your article; please answer all of these queries before sending the proof back to AIP.

Article checklist: In order to ensure greater accuracy, please check the following and make all necessary corrections before returning your proof.

1. Is the title of your article accurate and spelled correctly?
2. Please check affiliations including spelling, completeness, and correct linking to authors.
3. Did you remember to include acknowledgment of funding, if required, and is it accurate?

Location in article	Query / Remark: click on the Q link to navigate to the appropriate spot in the proof. There, insert your comments as a PDF annotation.
Q1	Please check that the author names are in the proper order and spelled correctly. Also, please ensure that each author's given and surnames have been correctly identified (given names are highlighted in red and surnames appear in blue).
Q2	In the sentence beginning "In Secs. II and III...," please confirm that "the following sections" refers to Secs. II and III.
Q3	Figures must be cited in numerical order; therefore, we have renumbered Figs. 1 and 2 as 2 and 1. Please check.
Q4	In the sentence beginning "In Subsection III B 2...," please confirm that "next subsection" refers to Sec. III B 2.
Q5	If e-print Ref. 20 has subsequently been published elsewhere, please provide updated reference information (journal title, volume number, and page number).
Q6	Please provide date and month for Ref. 45.
Q7	Please provide page number in Ref. 66.
	Please confirm ORCIDs are accurate. If you wish to add an ORCID for any author that does not have one, you may do so now. For more information on ORCID, see https://orcid.org/. Durgesh Kawale–0000-0002-3480-247X Jishnu Jayaraman Pouyan E. Boukany–0000-0002-2262-5795

Thank you for your assistance.

Biomicrofluidics ARTICLE scitation.org/journal/bmf

Microfluidic rectifier for polymer solutions flowing through porous media

Cite as: Biomicrofluidics 13, 000000 (2019); doi: 10.1063/1.5050201
Submitted: 27 July 2018 · Accepted: 26 January 2019 ·
Published Online: ■■ ■■ 2019

Durgesh Kawale,[1,2,a)] Jishnu Jayaraman,[1] and Pouyan E. Boukany[1,b)]

AFFILIATIONS

[1]Department of Chemical Engineering, Delft University of Technology, Van der Maasweg 9, 2629 HZ Delft, The Netherlands
[2]Department of Geoscience and Engineering, Delft University of Technology, Stevinweg 1, 2628 CN Delft, The Netherlands

[a)]Email: durgeshkawale@gmail.com
[b)]Electronic mail: P.E.Boukany@tudelft.nl

ABSTRACT

Fluidic rectification refers to anisotropic flow resistance upon changing the flow direction. Polymeric solutions, in contrast to Newtonian fluids, can exhibit an anisotropic flow resistance in microfluidic devices by tuning the channel shape at low Reynolds number. Such a concept has not been investigated in an anisotropic porous medium. We have developed a fluidic rectifier based on an anisotropic porous medium consisting of a periodic array of triangular pillars that can operate at a low Reynolds number. Rectification is achieved, when the type of high Weissenberg number elastic instabilities changes with the flow direction. The flow resistance differs across the two directions of the anisotropic porous medium geometry. We have identified the type of elastic instabilities that appear in both forward and backward directions. Particularly, we found a qualitative relation between the dead-zone instability and the onset of fluidic rectification.

I. INTRODUCTION

Understanding the flow of complex fluids such as colloidal dispersions, emulsions, liquid crystals, and polymer solutions through a porous medium plays a crucial role in various industrial and natural processes ranging from oil recovery, filtration, chemical reactors, polymer processing to blood, and interstitial flow in living tissues.[1,2] In general, these fluids exhibit complex flow behaviour, which distinguishes them from Newtonian fluids.[3,4] When a small amount of additive such as water-soluble polymer is added to water, the rheology of the resulting polymer solution can change drastically.[5] For instance, polymeric fluids often display strong viscoelastic effects at high deformation rates, due to a coupling between polymer conformation and flow field.[6] Macromolecules dispersed in a liquid such as water can be deformed and stretched when subjected to external forces in both shear and extensional flow fields.[7,8] The coil-stretch transition is one of the most fascinating phenomena of long polymer chains during flow, wherein a sudden increase in a polymer's extension occurs as the flow rate (or shear rate, $\dot{\gamma}$) exceeds a critical value.[9] Typically, the non-dimensional Weissenberg number ($\mathrm{Wi} = \dot{\gamma}\tau$) has been used to identify this transition. When the shear rate $\dot{\gamma}$ is higher than the reciprocal of polymer relaxation time τ, polymer molecules may stretch during flow.[10] In this regime, the elastic behavior dominates the rheological response, giving rise to a variety of elastic instabilities such as wall slip, shear banding, and flow inhomogeneity under different flow conditions.[11,12]

High-Wi number and low-Reynolds number ($\mathrm{Re} = \rho v d/\eta$, ρ is the fluid-density, v is the velocity, d is a characteristic length scale, and η is the shear-rate dependent viscosity) elastic instabilities occur in a wide class of flowing systems containing polymer solutions.[11,13–15] For instance, polymer solutions flowing through a porous medium can exhibit a significant increase in the pressure-drop measurements beyond a certain flow rate.[16] This increase in the pressure-drop, also known as the apparent shear thickening, has been observed experimentally[17–23] as well as modelled numerically,[24–27] occurs at low- to moderate-Re number and at high-Wi number. The origin of the elastic instability has been successfully linked to the dimensionless Mach number, $\mathrm{Ma} = \sqrt{\mathrm{WiRe}} \sim 1$.[17,23,28,29] The Ma number represents the ratio of the viscoelastic wave speed to the flow velocity.

Microfluidic devices are widely used for characterization of polymeric fluids, due to their ability to achieve high-Wi number with low inertial effects (low-Re number).[6,30,31] The typical length scale in these devices are few tens (or hundreds) of micrometers such that under flowing conditions, the Re number can be negligible, but the corresponding Wi could still be high enough for the elastic forces to dominate.[11,32] The small length scale also enables process intensification of a typical bulk chemical process via the so-called lab-on-a-chip devices. Lab-on-a-chip devices mostly refer to microfluidic chips that offer either some or all of the following benefits—short analysis-time, high sensitivity and resolution, low cost, and small operating sample volumes.[33] In addition, the performance of these devices depends on highly precise manipulation, transport, and control of small fluid volumes. In order to enable application-specific functionality, discrete microfluidic-modules are essential as they can be combined to design a complete lab-on-a-chip device.

Fluidic-rectifier is a lab-on-a-chip module that allows directional fluid-flow depending on the pressure gradient (or flow resistance) between two points. Its performance is quantified by *diodicity*,[34–40] defined as the pressure-drop ratio at a constant volumetric flow-rate, Q. These fluidic rectifiers operate via two mechanisms: the first mechanism utilizes a physical check-valve (active fluidic rectifier) and the second mechanism utilizes an anisotropic flow-geometry (passive fluidic rectifier). One of the earliest designs of an active fluidic rectifier consisted of a multilayer elastomer membrane covering a fluid-flow channel.[41,42] Subsequently, various other active fluidic rectifier designs were developed such as a flap and a diaphragm akin to a fluidic check-valve.[38,43,44] However, an active fluidic rectifier with moving parts is prone to mechanical failure. Jeon *et al.* reported polydimethylsiloxane (PDMS) diaphragm valves that were tested for 10^5 continuous cycles with water and their device performance did not show any noticeable failure. However, the possibility of a mechanical failure of a fluidic rectifier module might pose a limitation for developing robust lab-on-a-chip devices. Passive fluidic rectifiers on the other hand are simpler, more affordable, and do not contain any moving parts, making them potentially suitable as a fluidic rectifier modules over the active fluidic rectifiers.

Passive fluidic rectifiers are based on the difference in pressure-drop as the flow direction reverses in an anisotropic flow geometry such as a nozzle/diffuser shape. These devices utilize the high-Re inertial effects for Newtonian fluids[34,35,45–47] and low-Re, high-Wi elastic effects for non-Newtonian fluids.[36,39,40,48–51] Typically, microfluidic devices operate at a low-Re number (creeping flow) and consequently, the pressure-drop (δP) during flow of Newtonian fluid does not vary significantly as the flow direction reverses. In such situations, rectification could be achieved by adding a small quantity of additives (such as polymers or micelles) that impart viscoelasticity to the fluid. The low-Re and high-Wi number elastic instabilities of viscoelastic fluids like polymer solutions could be exploited to achieve passive rectification. In this spirit, microfluidic devices with single-flow-channels containing triangular,[49] hyperbolic,[36,50] and nozzle/diffuser shapes of varying angles[40] have been developed. In hyperbolic[36,50] and nozzle/diffuser shape,[40] rectification has been attributed to the difference in the pressure-drop due to two distinct types of corner vortexes as the flow direction reversed. In the triangular shape,[49] the rectification has been attributed to the presence of chaotic instabilities with corner vortices that seemed to appear and disappear randomly. Ejlebjerg Jensen *et al.* have resorted to topology optimization to determine the optimum layout of a passive fluidic rectifier for viscoelastic fluids. Their numerical study[51] has identified a design consisting of a nozzle/diffuser-like shape with an airfoil-like obstacle on the diffuser side of the flow geometry. In our earlier study, we have investigated the flow of polymer solutions through porous media consisting of periodic arrays of obstacles with different shapes.[17,28] The ability of a structured porous medium such that the flow resistance depends on the direction of flow, however, has not been explored until now.

Previously, several groups have investigated high-Wi and low-Re elastic instabilities occurring in a porous medium during the flow of polymer solutions relevant for polymer enhanced oil recovery.[17,18,52–54] Below $\mathrm{Wi} \sim 1$, the creeping flow is observed. As the Wi increases, the flow-field transitions into series of elastic instabilities. In the sequence of increasing Wi number, the stationary *dead-zone* elastic instability can be observed followed by the time-dependant dead-zone elastic instability. A dead-zone refers to a part in the entire flow field which appears to be stationary relative to the mean flow velocity, as confirmed by particle image velocimetry.[17,20,28] Both the stationary and the time-dependant instabilities of the dead-zones have been investigated previously by visualizing streamlines and particle image velocimetry. Furthermore, a detailed investigation of steady-state and dynamic velocity field in polymer solution flow through periodic array can also be found in previous literature.[21] The flow resistance of the stationary and the time-dependant instabilities depends on the shape of the obstacle in a microfluidic device.[17] The performance of a rectifier design based on a microfluidic device containing a periodic array of obstacles has not been investigated in the past. Previous experimental studies on polymer solution flow through microfluidic porous media containing uniform obstacles[17,18,20,21,53] and/or randomly oriented obstacles[27] focused on the apparent shear-thickening behaviour. Recent numerical studies showed that the various flow resistance curves in an array of cylinders can superimpose to a master curve when $\sqrt{k}$ is chosen as the length scale, where k is permeability.[55,56] In the current study, we present for the first time a passive fluidic rectifier design that exploits the apparent shear-thickening behaviour of an anisotropic porous medium. Our porous medium consists of triangular obstacles in a staggered layout. By measuring the pressure-drop and simultaneously visualizing the flow-streamlines, we investigate the flow-features that appear to affect rectification in our devices. In Secs. II and III, we first explain the experimental details and then present the results with specific discussions. Finally, we conclude by describing the relation between elastic instabilities and the rectification.

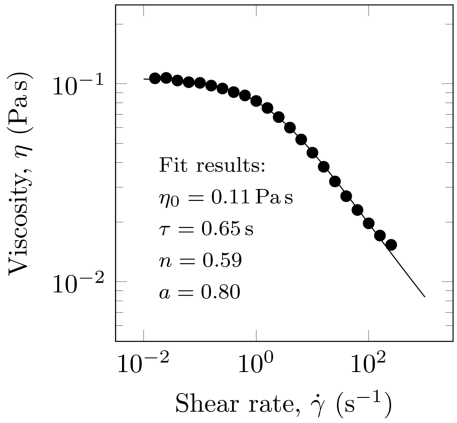

FIG. 1. Steady-shear viscosity of 0.3% (w/w) HPAM solution in 4% (w/w) NaCl, 100 ppm (w/w) NaN_3 at 22°. The solid line is a fit of experimental data (markers) to the Carreau-Yasuda model shown in Eq. (1).

II. MATERIALS AND METHODS

A. Polymer solution preparation and characterization

All microfluidic experiments with polymer solutions were performed using an aqueous solution of hydrolyzed polyacrylamide, HPAM 3530s (0.3% w/w, MW = 15×10^6 g mol^{-1}, 30% hydrolysis; SNF Floerger, France). The aqueous solvent used to disperse polymer granules consisted of 4% (w/w) NaCl to fix the ionic strength and 100 ppm (w/w) NaN_3 as a biocide. The procedure for preparing polymer solution is as follows: (1) filter de-ionized (DI) water through a 0.4 μm filter, (2) dissolve required amount of NaCl in the filtered DI water, (3) generate a vortex in the solvent by using a magnetic stirrer, (4) disperse polymer granules slowly in the vortex while avoiding polymer lump formation, (5) purge the bottle containing dispersed polymer granules with (nitrogen) N_2, and (6) lowering the stirring rate to ~200 rpm. Typically, the polymer granules were fully dissolved in ~24 h. The polymer solution used for all experiments was no more than a week old and every time the bottle was opened, it was purged with N_2.

We characterized the steady-shear viscosity of polymer solution in a Couette cell (cup ID = 30.36 mm, bob OD = 28 mm, gap = 1.18 mm) using the AR-G2 rheometer (TA Instruments). All experiments were performed at the room temperature, $T = (22 \pm 2)$°C. The polymer solution is shear-thinning as shown in Fig. 1. We fit the experimental steady-shear viscosity to the Carreau-Yasuda model shown below to calculate the polymer relaxation time.

$$\eta - \eta_\infty = (\eta_0 - \eta_\infty)\left[1 + (\tau\dot{\gamma})^a\right]^{\frac{n-1}{a}}. \quad (1)$$

Here, η is the viscosity, $\dot{\gamma}$ is the shear rate, η_0 is the zero-shear viscosity, τ is the polymer relaxation time, n is the power-law slope, and a controls the transition from zero-shear-viscosity plateau to the shear-thinning region. As we could not measure the infinite-shear viscosity, η_∞, we set it to the viscosity of the solvent (0.001 Pa s).

B. Microfluidic devices

The microfluidic devices used in the current study were fabricated using standard soft lithography techniques[17,57,58] and PDMS (polydimethylsiloxane; Sylgard® 184, Dow Corning Corporation). The devices consist of a central region with a periodic array of pillars. Two holes at the edges of the device serve as the inlet and the outlet. Two additional holes across the periodic array of pillars are used to connect the pressure sensors (see Fig. 2 for further details).

The fabricated microfluidic chip consists of an array of pillars representing the porous medium. The shape of these pillars, when observed from top/bottom of the device, resembles an equilateral triangle of side 262 μm. All pillars are spread over a 2D-array in a staggered layout [see Fig. 2(b)]. Table I lists the relevant dimensions of the microfluidic device used in this study.

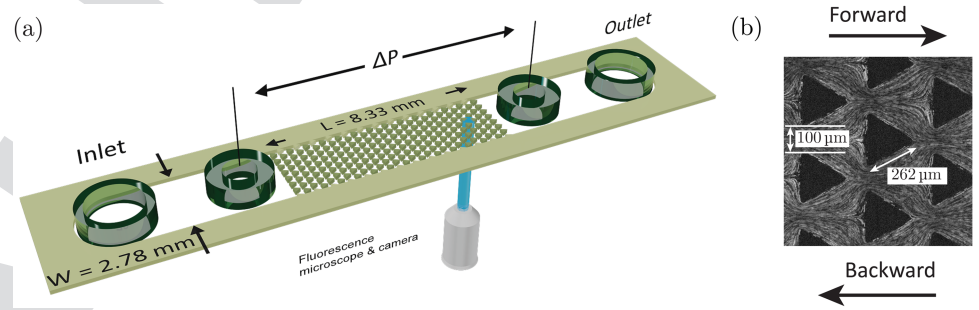

FIG. 2. (a) A Schematic of the anisotropic microfluidic device and the inverted microscope for streamline visualization and pressure drop measurement. The microfluidic device height is 100 μm, the width is 2.78 mm, and the periodic array length is 8.33 mm. (b) An optical fluorescent image of triangular pillars showing the two directions of flow—forward and backward, with respect to the pillar orientation. Each triangular pillar is an equilateral triangle with a side of 262 μm when viewed from top or bottom of the microfluidic device. The triangular pillars are spaced 100 μm apart from each other.

TABLE I. Dimensions of the microfluidic geometry.

Parameter	Value
Bed length	8.5 mm
Height	$(101 \pm 2)\,\mu$m
Width	2.75 mm
Pillar side	$262\,\mu$m
Porosity (φ)	0.75

C. Pressure drop measurement

The pressure is measured at the two pressure-taps located across the periodic array of pillars as shown in Fig. 2(a). As the pressure-taps were placed close to the array, the inlet/outlet contributions could be neglected. We confirmed that the flow field was not affected by placing the pressure-taps close to the array by visualizing flow without pressure taps (results not shown). The difference between these two point-pressure measurements is defined as the pressure-drop. We have used two piezoresistive silicon pressure sensors (HSCMRNT005PGAA5, Honeywell Sensing and Control) connected to a National Instruments data acquisition device. The data were logged using an in-house-developed LabVIEW program at 100 Hz. These pressure sensors measure the gauge pressure with each having a pressure range of 0 mbar to 330 mbar and an accuracy of 0.25% of the full scale span. A pressure pump (MFCS^{TM}, Fluigent GmbH) is used to calibrate our sensors. The instantaneous pressure value fluctuated with a standard deviation of 0.1 mbar around the mean.

D. Streamline visualization

In order to push fluids through the microfluidic device, we have used a syringe pump (PHD2000, Harvard Instruments) connected to a PTFE tubing (0.8 mm ID and 1.6 mm OD). The pressure sensors are connected to the pressure taps using a silicone tubing (see the supplementary material, Sec. S2 for additional details).

The streamlines are visualized using $1\,\mu$m fluorescent polystyrene beads (542/612 nm, Catalog no. R100, Thermo Scientific^{TM}) excited by UV light (X-Cite series 120Q, Lumen Dynamics). The microfluidic device has been integrated with an inverted microscope (Axiovert 100M, Carl Zeiss AG) fitted with a 10× (N.A. = 0.5) magnification objective and a high speed camera (Phantom v9.1, Vision Research Inc.). The focal point of the visualization has been adjusted to the middle plane along the channel height. The fluorescent particles sticking on the bottom surface of the microfluidic device are used a reference point to adjust the focal plane at the midpoint along the device height. The focal depth is $\delta z = \pm 7.4\,\mu$m for the combination of optics in setup.[59] Therefore, the streamlines visualized represent instabilities over a $\delta z = \pm 7.4\,\mu$m height around the middle plane of the device. The location along the device length was fixed near the downstream edge of the array. The streamlines have been visualized when the exposure time on the high speed camera was adjusted suitably at each flow rates (see Fig. S2 in the supplementary material). Further image processing was performed using an open source image processing program (ImageJ). The image quality was improved by adjusting the gamma, gain, brightness, and contrast.

E. Experimental procedure

After a microfluidic device is fabricated, it is integrated on the inverted microscope. We first flush the device with ethanol and ensure all the air in the device is displaced. The flow is switched to the polymer solution via a switching valve. All the flow lines are purged with corresponding liquids to displace any trapped air bubbles.

The pressure drop measurements and flow visualization experiments are performed simultaneously. For all experiments, the flow rate is increased stepwise while waiting for ~ 2 min to reach equilibrium at each step increase in the flow rate. To ensure a smooth pumping of liquids, we used small volume syringes (Hamilton Gastight 1000 series) at low flow rates. A new microfluidic device was used in each new experimental run. Reproducibility of the pressure drop measurements across independent experiments was found to be within ~2 mbar.

III. RESULTS AND DISCUSSION

A. Newtonian fluid flow

The pressure drop in the forward and the backward directions was measured for a Newtonian fluid (50% glycerol in DI water). Figure 3(a) shows the pressure drop in the forward and the backward directions for a non-inertial ($\mathrm{Re} \ll 1$) flow of the Newtonian fluid. We fit a general linear equation to the pressure drop *versus* the flow rate measurements to demonstrate the linearity. Typically, the Kozeny-Carmen equation or the Ergun equation is used to calculate the pressure drop in a porous medium.[2] However, these equations fail to predict pressure drop in microfluidic porous media.[60–63] The slope of pressure drop versus flow rate curves differs in the forward and in the backward directions. This difference, also known as directional permeability, is typical for an anisotropic pore-shape structure.[64–66] In striking contrast, the pressure-drop versus flow-rate slope in the forward/backward flow through single-channel fluidic rectifiers was found to be constant.[36,40,50]

We have also confirmed that the Newtonian fluid at the non-inertial condition $\mathrm{Re} \ll 1$ creeps around the periodic array of obstacles in both the forward and the backward directions. For example, Figs. 3(b) and 3(c) show the creeping flow streamlines during the Newtonian fluid flow at a flow rate of $10\,\mu\mathrm{l\,min^{-1}}$ ($\mathrm{Re} = 1.29 \times 10^{-2}$) and at $100\,\mu\mathrm{l\,min^{-1}}$ ($\mathrm{Re} = 1.29 \times 10^{-1}$). The length scale is taken as side of the triangle, $262\,\mu$m, for calculating Re. Note that the vertical lines in Fig. 3 are an artefact of our camera and the visualization setup. These lines do not affect the flow field.

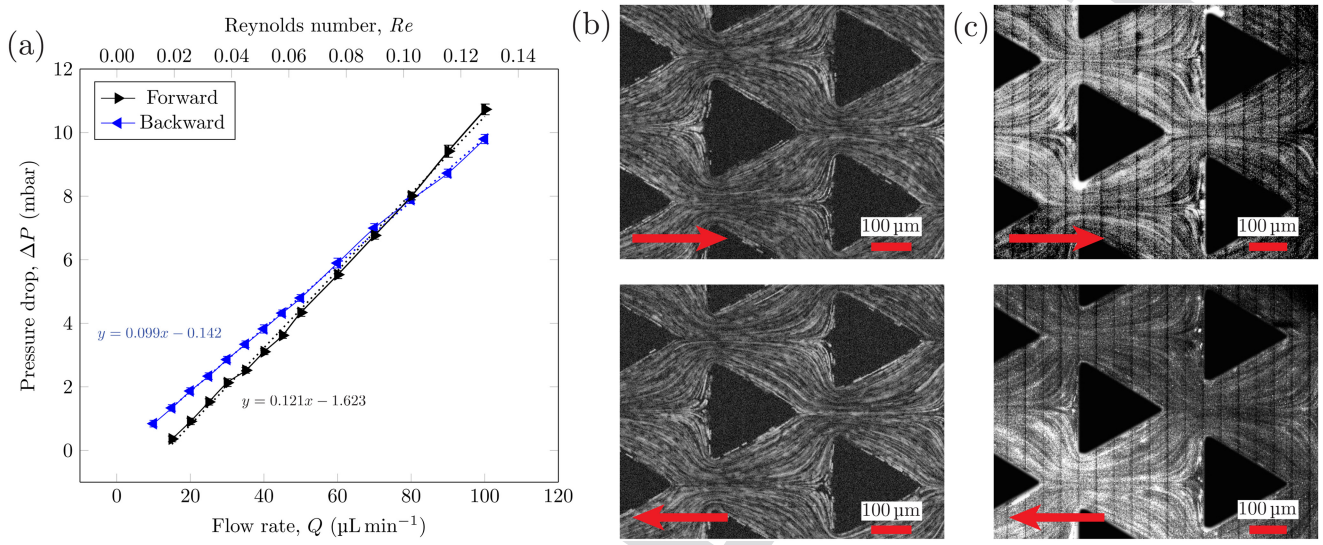

FIG. 3. (a) Newtonian fluid pressure drop measurements. (b) Streamlines of a Newtonian fluid flow at a flow rate of 10 μl min^{-1}, Re $= 1.29 \times 10^{-2}$. (c) Streamlines at a flow rate of 100 μm min^{-1}. Fluid: 50% glycerol in DI water.

B. Polymer fluid flow

1. Pressure-drop measurements

We have characterized the rectification performance of our porous medium fluidic rectifier by measuring the pressure-drop in the forward and in the backward directions. Figure 4(a) shows the pressure-drop versus the imposed flow rate and the corresponding Wi number. At low flow rates ($Q \lesssim 15\,\mu$l min^{-1}, Re $\lesssim 3.64 \times 10^{-3}$, Wi $\lesssim 6.5$), the pressure-drop is linearly dependent on the flow rate. Beyond $Q \sim 15\,\mu$l min^{-1}, the pressure-drop for both the forward and the backward flow direction becomes non-linear. The pressure-drop in the backward direction is higher than in the forward direction. The standard deviation of the pressure-drop fluctuations, S(ΔP) as a function of the imposed flow rate is shown in Fig. 4(b). Beyond $Q \sim 15\,\mu$l min^{-1}, the S(ΔP) for polymer flow in both backward and forward direction increases significantly compared to the Newtonian fluid flowing in the backward and the forward directions. Contrary to the difference between forward and backward mean pressure-drop, the S(ΔP) does not differ between the forward and the backward directions. At this point, it is instructive to compare the mean pressure-drop ratio in both directions by defining the *Diodicity* parameter at a constant flow rate as

$$\text{Diodicity}|_Q = \frac{\Delta P_{\text{backward}}}{\Delta P_{\text{forward}}}, \tag{2}$$

where $\Delta P_{\text{backward}}$ is the pressure drop in the backward direction and $\Delta P_{\text{forward}}$ is the pressure drop in the forward direction. In the linear regime of the pressure-drop versus flow rate curve, the diodicity is around 1 within experimental uncertainty [Fig. 4(c)]. In the non-linear regime, the diodicity increases gradually until a maximum value of ~ 2 [Fig. 4(c)]. We have further validated the rectification performance of our anisotropic porous medium microfluidic device by two additional polymer solutions, namely, (1) 0.4% HPAM 3530s and (2) 0.5% HPAM 3330 s. Both these polymer solutions demonstrated rectification with a maximum diodicity of 2.25 and 1.5, respectively (see the supplementary material, Sec. S1).

The maximum value of the diodicity depends on several factors such as fluid type, shape of obstacles, and aspect ratio.[36,39,40,49,50] For a single-channel fluidic rectifier, Sousa *et al.*[50] have showed that a hyperbolic wall shape exhibited higher diodicity than a triangular shape for a wide variety of fluid types. In a follow-up study, Sousa *et al.*[36] have found that the maximum diodicity in a hyperbolic single-channel fluidic rectifier can be increased by increasing the aspect ratio. They have been able to achieve a diodicity of ~ 6.5 for an aspect ratio of ~1.7. Typically, a single-channel fluidic rectifier with triangular shaped walls was found to have a maximum diodicity of ~2 with variations of around ± 0.5 depending on the fluid type.[40,49,50] Replacing the triangular pillars with hyperbolic wall shape might also lead to higher diodicity in the anisotropic porous medium geometry. Furthermore, porosity is another parameter that can be used to vary the diodicity in our device. Additional research is needed to address the precise effects of porosity on diodicity. In Subsection III B 2, we will discuss specific flow-field features over the entire range of the diodicity values. Q4

2. Flow visualization

The flow patterns in the linear regime (Re $\ll 1$, Wi < 1) of the pressure-drop versus flow rate are comparable to the

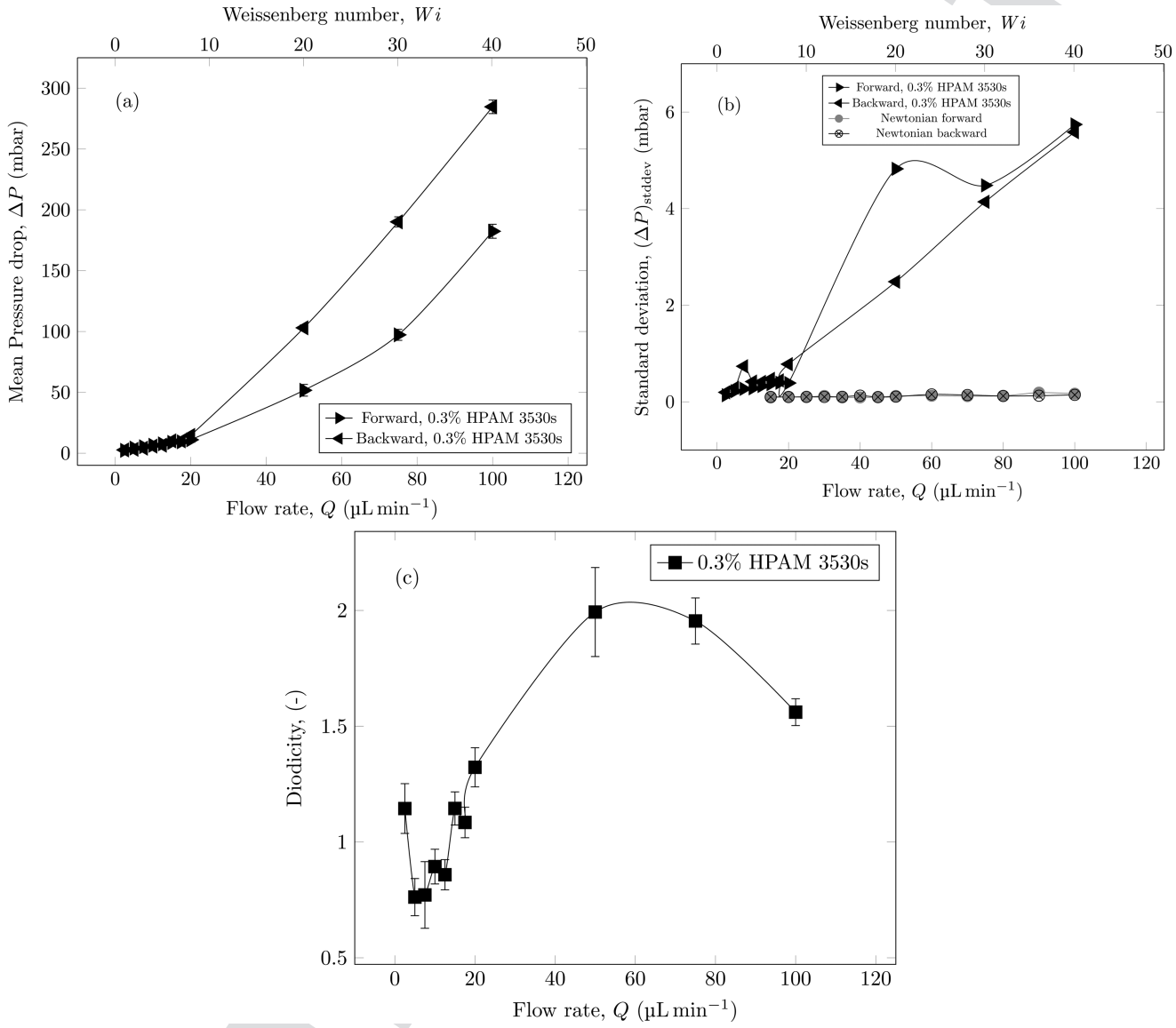

FIG. 4. Pressure drop was measured over a period of 300 s. (a) Mean pressure-drop and (b) the standard deviation versus the flow rate and the Wi number over the measurement period. The error bars in (a) show the standard deviation. (c) The diodicity as a function of the flow rate and the Wi number with error bars showing propagated error based on the pressure-drop fluctuation standard deviation.

Newtonian fluid flow streamlines [Fig. 3(b)] as shown in Figs. 5(a) and 5(b). In this situation, the streamlines in both directions are similar and appear symmetric along an axis parallel to the mean flow direction.

As the flow rate increases and the corresponding pressure-drop curve becomes non-linear, we observe elastic instabilities in both forward and backward directions. Above Wi $\sim$ 1, we first observe a *dead-zone* (DZ), which is a time-independent flow instability in the forward direction. A DZ instability consists of a large stagnation region in front of the obstacle where the local velocity magnitude is significantly lower than the velocity magnitude outside of the DZ. The velocity in the DZ is significantly lower than the velocity in the region surrounding the DZ as evident by the stationary fluorescent beads over multiple frames. Such a dead zone has also been previously observed in microfluidic porous media.[17,28] The dead-zones exhibit washing dynamics as it forms, first growing in size and then eventually being washed away (see movies in the supplementary material,

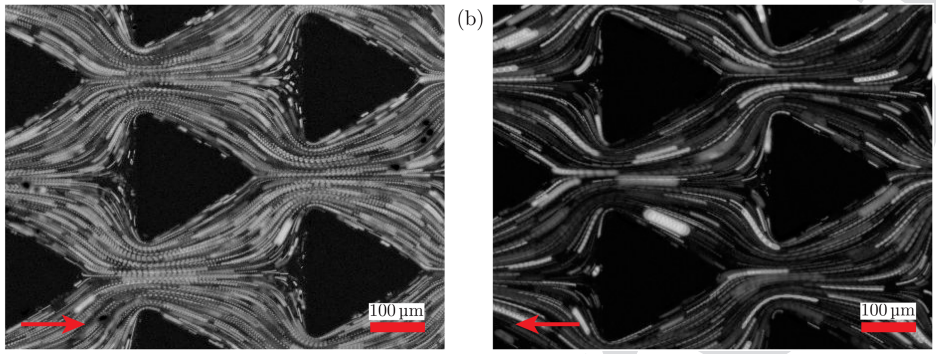

FIG. 5. Streamlines in the (a) forward and the (b) backward directions during the polymer solution flow at a flow rate of 1 μl min^{-1}, Re = 1.27 × 10^{-4}, and Wi = 0.4.

Sec. S4). The DZ washing frequency has been found to reach a steady value at ~4 mm distance from the upstream edge for the square and the circular staggered geometry.[17] Therefore, the flow field was visualized near the the downstream edge of the array of pillars where it had achieved psuedo-steady state. We have previously reported in detail the DZ instability in flow of shear-thinning polymer solutions through a periodic array of obstacles.[17] Here, we will emphasize the key differences between the DZ instabilities in the forward and the backward directions.

In the forward direction, a single-large DZ is formed upstream of every obstacle [see Fig. 6(a)]. For the range of flow-rates investigated in the current study, no downstream DZ was observed in the forward direction. In the backward directions, two small DZs are formed upstream of every obstacle [see Fig. 6(b)]. These two small DZs in the backward direction are located on the top and the bottom inclined edge of the triangular obstacle. The difference between the pressure-drop between the forward and the backward directions could be related the the dead-zone dynamics. In the forward direction, the large upstream dead-zone has a stabilising effect on the fast moving streamlines in between the pillars [Figs. 6(a) and 6(c)] with limited expansions and contractions. On the other hand, the absence of a large upstream dead-zone in the backward direction allows the flow field to experience relatively greater contractions and expansions than in the forward direction. These elastic stresses are amplified at higher Wi number giving rise to the anisotropic flow resistance. In general, the increase in flow resistance at high Wi number (for both forward and backward directions) has been linked to shear dominated flow features.[55,56,67] Therefore, the shear dominated flow features in the backward direction are perhaps relatively stronger than those in the forward direction. Previous studies in single-channel rectifiers with a nozzle/diffuser geometry also found flow resistance in the backward direction to be higher than in the forward direction.[36,40,68] The upstream inertio-elastic DZ time dependent instability has been linked to originate at Ma ~ 1.[17,23,28,29] The DZ instability in both forward and backward directions also originates at Ma ~ 1 in agreement with the previous observations. The image quality is compromised at high flow rates in the backward direction due to a higher number of fluorescent beads sticking on the top and the bottom surface of the microfluidic device. In order to reduce the uncertainty of backward upstream DZ area measurement, we considered the DZ areas that were distinguishable over multiple frames. The distinguishing aspect of the backward upstream DZ is the displacement of bright fluorescent beads along a vortex near the triangular pillar edges. A backward downstream DZ was observed in the backward direction at flow rates higher than ~ 75 μl min^{-1} (Wi ~ 32). At lower flow rates, no backward downstream DZ has been observed. The single-large DZ in the forward direction grows and wobbles in a direction perpendicular to the average flow direction, until it washes away eventually. The entire DZ growth-wobbling-washing cycle repeats periodically. Figure 6(c) shows the wobbling motion of DZs over time for the forward direction, and Fig. 6(d) shows the relative lack of DZ motion over time for the backward direction.

In order to evaluate the relation of the DZs in both forward and backward directions, we have measured the DZ area from the streamline images. We have measured three types of areas—(1) the area of the upstream single-large DZ in the forward direction, (2) the area of the upstream two DZs in the backward direction, and (3) the area of the downstream DZ in the backward direction [as represented schematically in Fig. 7(a)]. All types of DZ areas refer to the largest observed area over its lifetime. In Fig. 7(b), we plot the DZ areas normalized with the top surface area of the triangular obstacle over a range of flow rates. Note that in each case, the area of 10 DZs is measured, and Fig. 7(b) shows the average value with the error bars showing the standard deviation. We can see that at a flow rate of 20 μl min^{-1} all the DZ areas are the same (~ 0.4) with the corresponding diodicity of ~ 1 [Fig. 4(b)]. As the flow rate is increased to 50 μl min^{-1}, the upstream DZ area in the forward direction increased to ~ 0.6, whereas the upstream DZ area in the backward direction remains constant at ~ 0.4. Additional information on marking the DZ area on the streamline images is shown in the supplementary material (Sec. S3). The corresponding diodicity has also increased to

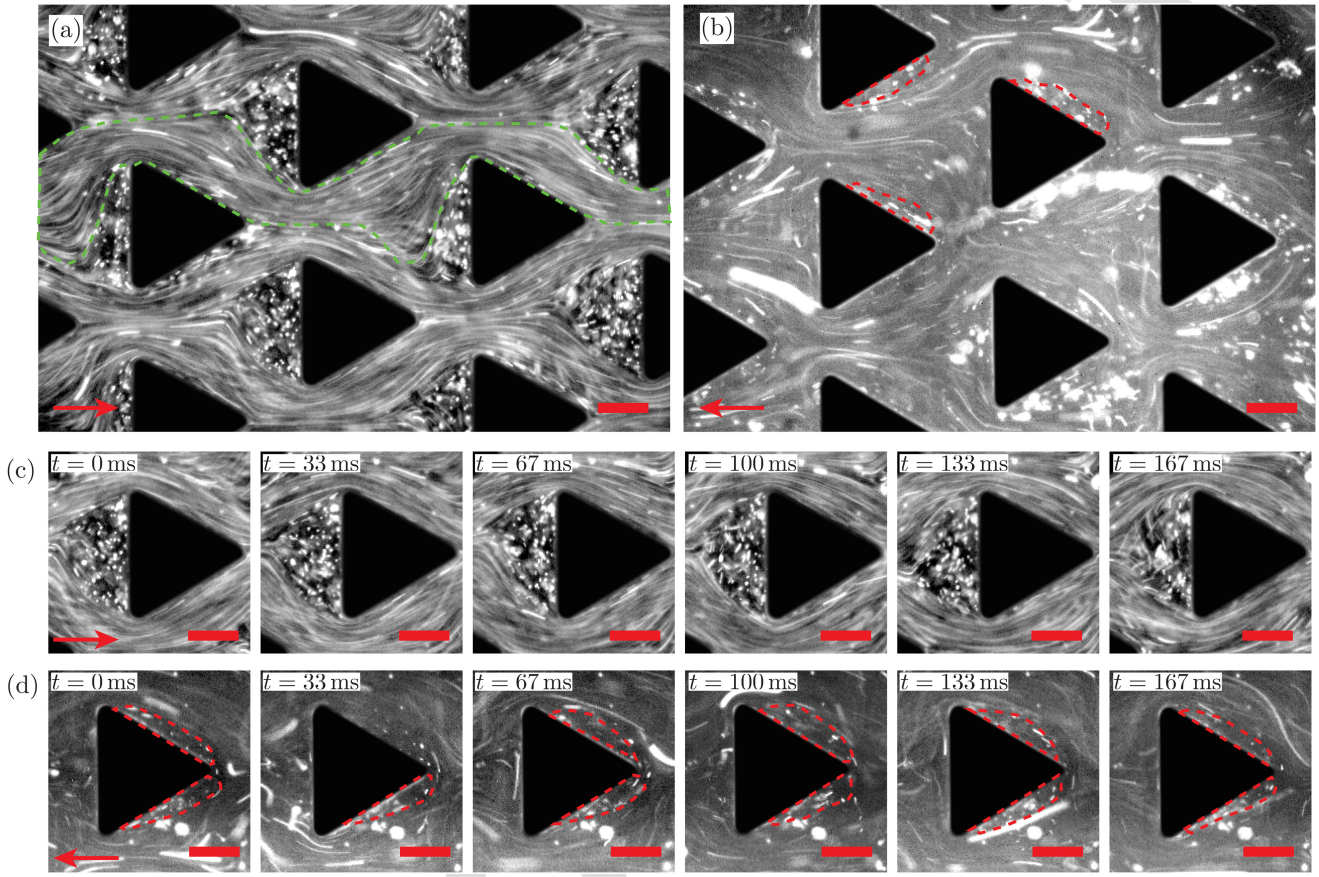

FIG. 6. The streamline images of polymer solution flow in the (a) forward and the (b) backward directions showing persistent dead zones. (c) shows the dead zone wobbling in the forward direction, whereas (d) shows the dead zone in the backward direction. The green dotted line in (a) shows flow-field channelling due to DZ formation. The red dotted regions in (b) and (d) show the upstream DZ in the backward direction. Flow rate $= 50\,\mu l\,min^{-1}$, Re $= 1.85 \times 10^2$, and Wi $= 21.5$ (max diodicity). Scale bar $= 100\,\mu m$.

~ 2 [Fig. 4(b)]. We do not observe a downstream DZ in the backward direction at this flow rate. As the flow rate is further increased to $75\,\mu l\,min^{-1}$ and to $100\,\mu l\,min^{-1}$, the upstream DZ area in the forward direction remains constant at ~ 0.6 and the upstream DZ area in the backward direction also remains constant at ~ 0.4. At these flow rates, we observe the formation of the downstream DZ in the backward direction. When we add the upstream DZ area and the downstream DZ area in the backward direction, the total DZ area in the backward direction matches with the upstream DZ area in the forward direction (also see Sec. S3 in supplementary material). Correspondingly, the diodicity under this condition also decreases to ~ 1.5 [Fig. 4(b)]. The diodicity values appear to be related qualitatively to the DZ areas in the following manner—higher diodicity values are correlated to a higher difference between the total DZ area in the forward and the backward directions. One of the consequences of a DZ in the forward direction is to confine the flow between the pillars in channels [for instance, see the green dotted region in Fig. 6(a)]. Such a channeling limits the contraction and expansions of the fluid compared to the flow in the backward direction between $20\,\mu l\,min^{-1}$ and $50\,\mu l\,min^{-1}$, causing an increase in the diodicity. Above $50\,\mu l\,min^{-1}$, a downstream DZ is formed thereby minimizing the contraction and expansion of the fluid. Formation of the downstream DZ is accompanied by a decrease in diodicity. In future, it will be insightful to study the impact of microfluidic anisotropic porous medium geometry on DZ shape and on diodicity.

In general, our observation of a higher pressure-drop in the direction of gradual-contraction to rapid-expansion (backward direction) is consistent with previous experiments. For single-channel experiments, the higher pressure-drop has also been observed when the flow moved from a gradually contracting to a rapidly expanding direction.[36,40,49,50] In single-channel experiments, the reason for observing rectification was reported because of the strong extensional flow in

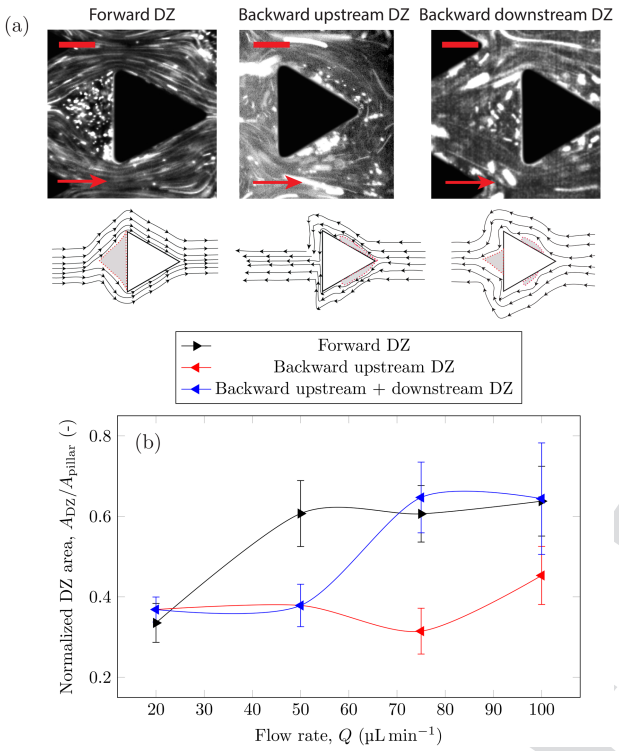

FIG. 7. (a) A representative streamline image and its corresponding schematic showing (left) the forward DZ at $Q = 50\,\mu l\,min^{-1}$, (middle) backward upstream DZ at $Q = 50\,\mu l\,min^{-1}$, and (right) the backward downstream DZ at $Q = 100\,\mu l\,min^{-1}$. (b) The normalized DZ area for the three DZs as shown in (a) over the range of flow rates of polymer solution. Solid line is shown as a guide to the eye. Scale bar = 100 μm.

the backward direction compared to the forward direction, with forward/backward direction referred according to definition in this manuscript.

IV. CONCLUSIONS

We have investigated low-Re, high-Wi fluidic rectification in an anisotropic porous medium consisting of a periodic array of triangles. The anisotropic geometry has produced different flow-fields as the flow direction has been reversed. At low flow rates, the creeping flow has been observed in both forward and backward flow directions. At a certain onset flow rate, (Wi ~ 1.0) the flow field becomes unstable. These instabilities are well correlated with the rapid increase in the flow resistance typically observed for polymer solutions flowing through porous media.[17,18,20,28,54] In agreement with our previous studies, we show that as the polymer solutions flow through anisotropic porous medium in both forward/backward directions, the flow field transitions to a time-dependent elastic instability with the pressure-drop fluctuations increasing simultaneously at Ma ~ 1.0. The differences in the time-dependent elastic instabilities in the forward and the backward directions lead to a difference in the value of pressure-drop. The backward to forward pressure-drop ratio can vary up to a factor of 2 with the flow rate. In addition, we have discovered that the area of the dead-zone type instability appears to be qualitatively related to the diodicity. We believe that this microfluidic rectifier can be used and integrated as passive valves in generic microfluidic porous medium for broad applications ranging from rheological characterization to cell/bio-particle separation in lab-on-a-chip technologies.[69]

SUPPLEMENTARY MATERIAL

See the supplementary material for (1) rectification behaviour with additional polymer solutions, (2) experimental set-up of flow visualization, (3) additional data on the streamline visualization at a flow rate of 50 and 100 $\mu l\,min^{-1}$ (at room temperature), (4) movies of flow in the forward and the backward directions, and (5) PIV characterization in the creeping flow regime.

ACKNOWLEDGMENTS

This research forms part of the research programme of the Dutch Polymer Institute (DPI), Project No. 736n. A part of this study was also supported by the European Research Council under the European Seventh Framework Programme (No. FP/2007-2013)/ERC Grant Agreement No. 337820 (to P.E.B.). The authors thank Shaurya Sachdev and Dayinta Perrier for critical reading of the manuscript.

REFERENCES

[1]A. Anbari, H.-T. Chien, S. S. Datta, W. Deng, D. A. Weitz, and J. Fan, Small **14**, 1703575 (2018).
[2]F. A. Dullien, *Porous Media: Fluid Transport and Pore Structure* (Academic Press, San Diego, 1992), Vol. 2.
[3]*Dynamics of Polymeric Liquids*, edited by R. B. Bird, 2nd ed. (Wiley, New York, 1987), p. 2.
[4]S.-Q. Wang, *Nonlinear Polymer Rheology: Macroscopic Phenomenology and Molecular Foundation* (John Wiley & Sons, 2018).
[5]H. A. Barnes, J. F. Hutton, and K. Walters, *An Introduction to Rheology* (Elsevier, 1989).
[6]L. Rems, D. Kawale, L. J. Lee, and P. E. Boukany, Biomicrofluidics **10**, 043403 (2016).
[7]T. T. Perkins, D. E. Smith, and S. Chu, Science **276**, 2016 (1997).
[8]D. E. Smith, H. P. Babcock, and S. Chu, Science **283**, 1724 (1999).
[9]T. T. Perkins, S. R. Quake, D. E. Smith, and S. Chu, Science **264**, 822 (1994).
[10]P. G. DeGennes, *Scaling Concepts in Polymer Physics* (Cornell University Press, 1979).
[11]R. G. Larson, Rheol. Acta **31**, 213 (1992).
[12]*Rheology: Principles, Measurements, and Applications*, edited by C. W. Macosko (VCH, New York, 1994), p. 550.
[13]D. V. Boger, Annu. Rev. Fluid Mech. **19**, 157 (1987).
[14]E. S. Shaqfeh, Annu. Rev. Fluid Mech. **28**, 129 (1996).
[15]D. F. James, Annu. Rev. Fluid Mech. **41**, 129 (2009).
[16]L. W. Lake, R. Johns, W. Rossen, and G. Pope, *Fundamentals of Enhanced Oil Recovery* (Society of Petroleum Engineers, 2014).
[17]D. Kawale, E. Marques, P. L. J. Zitha, M. T. Kreutzer, W. R. Rossen, and P. E. Boukany, Soft Matter **13**, 765 (2017).

[18]A. Clarke, A. M. Howe, J. Mitchell, J. Staniland, L. Hawkes, and K. Leeper, Soft Matter **11**, 3536 (2015).
[19]J. Odell and S. Haward, Rheol. Acta **47**, 129 (2008).
[20]S. De, J. van der Schaaf, N. Deen, J. Kuipers, E. Peters, and J. Padding, preprint arXiv:1607.03672 (2016).
[21]S. De, J. van der Schaaf, N. Deen, J. Kuipers, E. Peters, and J. Padding, Phys. Fluids **29**, 113102 (2017).
[22]Y. Zhao, A. Q. Shen, and S. J. Haward, Soft Matter **12**, 8666 (2016).
[23]X. Shi, S. Kenney, G. Chapagain, and G. F. Christopher, Rheol. Acta **54**, 805 (2015).
[24]R. Poole, M. Alves, and P. Oliveira, Phys. Rev. Lett. **99**, 164503 (2007).
[25]D. Richter, G. Iaccarino, and E. S. Shaqfeh, J. Fluid Mech. **651**, 415 (2010).
[26]S. De, S. Das, J. Kuipers, E. Peters, and J. Padding, J. Nonnewton. Fluid Mech. **232**, 67 (2016).
[27]S. De, J. Kuipers, E. Peters, and J. Padding, Phys. Rev. Fluids **2**, 053303 (2017).
[28]D. Kawale, G. Bouwman, S. Sachdev, P. L. Zitha, M. T. Kreutzer, W. R. Rossen, and P. E. Boukany, Soft Matter **13**, 8745 (2017).
[29]S. Kenney, K. Poper, G. Chapagain, and G. F. Christopher, Rheol. Acta **52**, 485 (2013).
[30]X. Hu, P. E. Boukany, O. L. Hemminger, and L. J. Lee, Macromol. Mater. Eng. **296**, 308 (2011).
[31]S. J. Haward, Biomicrofluidics **10**, 043401 (2016).
[32]G. M. Whitesides, Nature **442**, 368 (2006).
[33]V. Hessel, J. C. Schouten, and A. Renken, *Micro Process Engineering: A Comprehensive Handbook* (John Wiley & Sons, 2009), Vol. 1
[34]C.-H. Tsai, C.-H. Lin, L.-M. Fu, and H.-C. Chen, Biomicrofluidics **6**, 024108 (2012).
[35]C.-H. Tsai, C.-P. Yeh, C.-H. Lin, R.-J. Yang, and L.-M. Fu, Microfluid. Nanofluidics **12**, 213 (2012).
[36]P. C. Sousa, F. T. Pinho, M. S. Oliveira, and M. A. Alves, RSC Adv. **2**, 920 (2012).
[37]R. D. Sochol, A. Lu, J. Lei, K. Iwai, L. P. Lee, and L. Lin, Lab. Chip **14**, 1585 (2014).
[38]J. Loverich, I. Kanno, and H. Kotera, Microfluid. Nanofluidics **3**, 427 (2007).
[39]K. Ejlebjerg Jensen, P. Szabo, F. Okkels, and M. Alves, Biomicrofluidics **6**, 044112 (2012).
[40]N.-T. Nguyen, Y.-C. Lam, S.-S. Ho, and C. L.-N. Low, Biomicrofluidics **2**, 034101 (2008).
[41]M. A. Unger, H.-P. Chou, T. Thorsen, A. Scherer, and S. R. Quake, Science **288**, 113 (2000).
[42]J. R. Anderson, D. T. Chiu, R. J. Jackman, O. Cherniavskaya, J. C. McDonald, H. Wu, S. H. Whitesides, and G. M. Whitesides, Anal. Chem. **72**, 3158 (2000).
[43]N. L. Jeon, D. T. Chiu, C. J. Wargo, H. Wu, I. S. Choi, J. R. Anderson, and G. M. Whitesides, Biomed. Microdevices **4**, 117 (2002).
[44]J. J. Loverich, I. Kanno, and H. Kotera, Lab. Chip **6**, 1147 (2006).
[45]N. Tesla, "Valvular conduit," U.S. patent 1,329,559 (■ 1920).
[46]E. Stemme and G. Stemme, Sens. Actuators A Phys. **39**, 159 (1993).
[47]T. Gerlach and H. Wurmus, Sens. Actuators A Phys. **50**, 135 (1995).
[48]A. Groisman, M. Enzelberger, and S. R. Quake, Science **300**, 955 (2003).
[49]A. Groisman and S. R. Quake, Phys. Rev. Lett. **92**, 094501 (2004).
[50]P. Sousa, F. Pinho, M. Oliveira, and M. Alves, J. Nonnewton. Fluid Mech. **165**, 652 (2010).
[51]K. Ejlebjerg Jensen, P. Szabo, and F. Okkels, Appl. Phys. Lett. **100**, 234102 (2012).
[52]B. Khomami and L. D. Moreno, Rheol. Acta **36**, 367 (1997).
[53]A. Machado, H. Bodiguel, J. Beaumont, G. Clisson, and A. Colin, Biomicrofluidics **10**, 043507 (2016).
[54]A. M. Howe, A. Clarke, and D. Giernalczyk, Soft Matter **11**, 6419 (2015).
[55]S. De, J. Kuipers, E. Peters, and J. Padding, Soft Matter **13**, 9138 (2017).
[56]S. De, J. Kuipers, E. Peters, and J. Padding, J. Nonnewton. Fluid Mech. **248**, 50 (2017).
[57]D. C. Duffy, J. C. McDonald, O. J. A. Schueller, and G. M. Whitesides, Anal. Chem. **70**, 4974 (1998).
[58]J. C. McDonald and G. M. Whitesides, Acc. Chem. Res. **35**, 491 (2002).
[59]C. Meinhart, S. Wereley, and M. Gray, Meas. Sci. Technol. **11**, 809 (2000).
[60]N. S. K. Gunda, J. Joseph, A. Tamayol, M. Akbari, and S. K. Mitra, Microfluid. Nanofluidics **14**, 711 (2013).
[61]J. Joseph, N. S. K. Gunda, and S. K. Mitra, Chem. Eng. Sci. **99**, 274 (2013).
[62]S. Le Gac, J. Carlier, J.-C. Camart, C. Cren-Olivé, and C. Rolando, J. Chromatogr. B **808**, 3 (2004).
[63]F. J. Valdes-Parada, J. A. Ochoa-Tapia, and J. Alvarez-Ramirez, Phys. A Stat. Mech. Appl. **388**, 789 (2009).
[64]P. A. Rice, D. J. Fontugne, R. G. Latini, and A. J. Barduhn, Ind. Eng. Chem. **62**, 23 (1970).
[65]P. Renard, A. Genty, and F. Stauffer, J. Geophys. Res. Solid Earth **106**, 26443 (2001).
[66]J.-B. Clavaud, A. Maineult, M. Zamora, P. Rasolofosaon, and C. Schlitter, J. Geophys. Res. Solid Earth **113**, ■ (2008).
[67]D. F. James, R. Yip, and I. G. Currie, J. Rheol. **56**, 1249 (2012).
[68]A. Groisman and V. Steinberg, New J. Phys. **6**, 29 (2004).
[69]G. R. Pesch, M. Lorenz, S. Sachdev, S. Salameh, F. Du, M. Baune, P. E. Boukany, and J. Thöming, Sci. Rep. **8**, 10480 (2018).